

Atomic model for the membrane-embedded V_O motor of a eukaryotic V-ATPase

Mohammad T. Mazhab-Jafari¹, Alexis Rohou², Carla Schmidt^{3,4}, Stephanie A. Bueler¹, Samir Benlekbir¹, Carol V. Robinson³, and John L. Rubinstein^{1,5,6}

1. Molecular Structure and Function Program, The Hospital for Sick Children, Toronto, M5G 0A4, Canada.
 2. Janelia Research Campus, Howard Hughes Medical Institute, Ashburn, 20147, United States.
 3. Department of Chemistry, Physical and Theoretical Chemistry Laboratory, University of Oxford, Oxford, OX1 3QZ, United Kingdom.
 4. Current address: Interdisciplinary research center HALOmeme, Martin Luther University Halle-Wittenberg, 06120 Halle / Saale, Germany.
 5. Department of Medical Biophysics, University of Toronto, Toronto, Canada M5G 1L7
 6. Department of Biochemistry, University of Toronto, M5S 1A8, Canada.
- Correspondence to: john.rubinstein@utoronto.ca

Summary

Vacuolar-type ATPases (V-ATPases) are ATP-powered proton pumps involved in processes including endocytosis, lysosomal degradation, secondary transport, TOR signaling, osteoclast function, and kidney function. ATP hydrolysis in the soluble catalytic V₁ region drives proton translocation through the membrane-embedded V_O region via rotation of a rotor subcomplex. Variability in the structure of the intact enzyme has prevented construction of an atomic model for the membrane-embedded motor of any rotary ATPase¹⁻⁵. We induced dissociation and auto-inhibition of the V₁ and V_O regions of V-ATPase by starving yeast^{6,7}, allowing us to obtain a ~3.9 Å resolution electron cryomicroscopy map of the V_O complex and build atomic models for the majority of its subunits. The analysis reveals the structures of subunits a₃c'c''de and a protein that we identify and propose to be a new subunit (subunit f). A large cavity between subunit a and the c-ring creates a cytoplasmic half-channel for protons. The c-ring has an asymmetric distribution of proton-carrying Glu residues, with the Glu residue of subunit c'' interacting with Arg735 of subunit a. The structure suggests sequential protonation and deprotonation of the c-ring, with ATP-hydrolysis-driven rotation causing protonation of a Glu at the cytoplasmic half-channel and subsequent deprotonation of a Glu residue at a luminal half-channel.

Main text

Overall structure

Following starvation-induced dissociation of the V₁ and V_O regions of V-ATPase, the auto-inhibited V_O complex is significantly more structurally homogeneous than in the intact V-ATPase¹. Our 3D electron cryomicroscopy (cryo-EM) map reveals the structure of the intact V_O complex (Fig. 1A-C, Supplementary Fig. 1, Supplementary Table 1) with an overall resolution of 3.9 Å (Supplementary Fig. 2). While resolution is variable throughout the map (Supplementary Fig. 2C) side-chain densities are apparent for most

of the α -helices in the complex, allowing construction of an atomic model (Fig. 1D, Supplementary Fig. 3). A few regions (e.g. supplementary Fig. 3G) only have sufficient resolution to model large side chains, which still allows the protein sequence to be placed in register in the map. Resolution was worst for the soluble domain of subunit a where it contacts subunit d, which we modeled entirely as poly-alanine. The map reveals the structures of the $c_8c'_c''$ -ring (Fig. 1A, pink, deep pink, and purple), subunit a (Fig. 1, green), subunit d (Fig. 1A, cyan), and two additional proteins. These additional components were detected in a lower-resolution analysis of the intact V-ATPase complex^{1,5} but can be seen here to consist of two trans-membrane α -helices each (Fig. 1B and C, blue and red-brown). Both of these proteins appear to be stoichiometric components of the complex, as judged by their relative density in the map. One of these subunits (red-brown in Fig. 1B and C) abuts α -helix 2 and the loop connecting α -helices 7 and 8 of subunit a. The other protein is an α -helical hairpin that contacts α -helix 1 of subunit a (blue in Fig. 1B and C). These two proteins are discussed in more detail below.

Subunit d sits on top of the c-ring, linking the V_1 and V_O parts of the central rotor. As seen previously in an ~ 18 Å resolution map of the V_O complex⁸, subunit d sits deeper within the c-ring in the V_O complex than in the intact V-ATPase. The N-terminal domain of subunit a reorients in the V_O complex relative to its position in the intact V-ATPase^{1,9} to contact subunit d. When separated from the V_1 region, the V_O complex is impermeable to protons^{6,7}. Interaction of subunit a from the stator part of the complex with subunit d from the rotor is expected to inhibit rotation and proton permeability. However, the V_O complex remains impermeable to protons even when subunit d or the N-terminal domain of subunit a are removed^{8,10}. Furthermore, we also identified a 3D class that lacks subunit d but otherwise appears to have almost the same structure as the intact V_O complex (Supplementary Fig. 4). Consequently, the movement of the N-terminal domain of subunit a, relative to its position in the intact V-ATPase, cannot be due to interaction with subunit d.

Subunit a

The fold of subunit a is consistent with the fold predicted from lower-resolution cryo-EM of the intact V-ATPase combined with evolutionary covariance analysis⁵. The subunit contains 8 membrane-embedded α -helices with structured loops connecting some of these α -helices. The membrane-embedded domain of subunit a starts with a pair of short α -helices that do not fully cross the lipid bilayer (Fig. 1B and C, α -helices a_1 and a_2). Four subsequent trans-membrane α -helices (a_3 to a_6) produce a central layer in the subunit structure, which terminates with two long and highly-tilted trans-membrane α -helices that contact the c-ring (a_7 and a_8) and are characteristic of rotary ATPases^{1,2,5,11}. No density was detected for the loop between residues 659 and 709, which is the region with the least sequence similarity between different isoforms of subunit a⁵. The lack of density for this loop suggests that it is mobile in the structure. Another loop (residues 481 to 523) also could not be modeled, although a region of low-resolution density in the map (Fig. 1B, semi-transparent grey density) probably corresponds to this loop and to parts of the two small membrane-embedded proteins in the V_O complex.

The c-ring

Unlike the c-ring of F-type ATP synthases and bacterial V/A-ATPases, the proton-carrying ring of the eukaryotic V-ATPase is hetero-oligomeric. The *S. cerevisiae* V-ATPase $c_8c'c''$ -ring has 40 trans-membrane α -helices arranged into an inner ring and outer ring of 20 α -helices each (Fig. 2)^{1,12}. Each c, c', and c'' subunit contributes 4 α -helices to the c-ring, two to the inner ring and two to the outer ring. The cryo-EM map shows two additional α -helices that pass through the $c_8c'c''$ -ring (Fig. 2B, purple '*'). These α -helices can be attributed to 56 residues at the N terminus of subunit c''¹³, most of which are not necessary for proton translocation¹⁴, and correspond to density seen previously within the c-ring¹⁵ and upon re-examination of the intact V-ATPase maps¹. The first additional α -helix is adjacent to subunit $c_{(1)}$ and the second is near the center of the c-ring with a clear connection to the rest of subunit c''. Although map resolution is limited in this region, it is sufficient to register the sequence of the α -helices (Supplementary Fig. 3B). This structure for subunit c'' differs from a crystal structure of a bacterial hybrid "F/V" c-ring, where a single additional N-terminal helix lay across the cytoplasmic surface of the ring¹⁶. Subunit c'' serves as the main contact between subunit d and the c-ring (Fig. 1A, lower, cyan '*'), making it critical for the transmission of ATP-driven rotation of subunits D and F of the V_1 region to the c-ring of the V_0 region. Comparison to the lower-resolution cryo-EM maps of the intact V-ATPase¹ (Supplementary Fig. 5A-C) shows that the V_0 complex is in the least populated, and likely least stable, of the three rotational states identified for the intact enzyme (Supplementary Fig. 5D). Therefore, subunit c'' apparently marks the position of the c-ring from which the complex can disassemble and reassemble^{6,7}. An additional surprising feature of the subunit c'' structure is the location of its essential proton-carrying Glu residue¹³. Each c, c', and c'' subunit has a single proton-carrying Glu residue (Glu137, 145, and 108, respectively¹³), giving 10 proton carrying-residues for the 20 outer α -helices of the ring. Remarkably, the Glu residue of subunit c'' is on its 2nd ring-forming α -helix, while in subunits c and c' it is found on their 4th ring-forming α -helix. This arrangement gives an irregular distribution of acidic proton-carrying Glu residues, rather than having proton-binding sites on alternating α -helices (Fig. 2B, right side, red dots). The two adjacent negative charges of subunits c'' and $c_{(1)}$ in contact with subunit a may determine the disassembly and reassembly competent conformation of the enzyme.

Interface of subunit a and c-ring

Trans-membrane proton pumping is thought to occur via two offset half-channels: a cytoplasmic half-channel that protonates Glu residues of the c-ring and a luminal half-channel that deprotonates Glu residues^{17,18}. The cytoplasmic half-channel, which leads to Glu108 of subunit c'', is readily apparent from inspection of the model as a deep cavity between the c-ring and the two highly tilted α -helices of subunit a (Fig. 3A and B, blue density and arrow). At its opening to the cytoplasm, this cavity is almost 20 Å across and 10 Å wide and is expected to be filled with water¹⁹, providing direct access for protons from the cytoplasm to Glu108. The location of this channel at the interface of subunit a and the c-ring is consistent with biochemical experiments²⁰⁻²² and indentations in the detergent micelles of lower-resolution cryo-EM density maps of the F-, V/A-, and V-type

ATPases^{1-3,5}. The position of the cytoplasmic half-channel places it in close proximity to the loop of 51 residues between α -helices a_5 and a_6 (659 to 709), which contains 21 charged residues and substantial coevolution of residues⁵. This loop may be involved in modulating access to the half-channel⁵. The location of the luminal half-channel is less obvious. A slight gap in the detergent micelle was suggested from inspection of lower-resolution cryo-EM maps²³ and a path involving the first and second membrane-embedded α -helices of subunit a (a_1 and a_2 in Fig. 1C) was suggested by considering residues conserved across species⁵. This presumed location of the luminal half-channel places its exit near the region of un-modeled density in the cryo-EM map (Fig. 3A, grey mesh). However, a clear path through the protein from the center of the lipid bilayer to its luminal surface is not readily apparent from the model and could not be detected by automated identification of potential pore-lining residues²⁴ or searching for gaps in the protein²⁵. It should be recalled that the dissociated V_O region is auto-inhibited and does not allow proton translocation^{6,8} and the luminal half-channel may not exist in this state. Alternatively, the luminal half-channel may remain closed in proton-pumping V-ATPases until it is needed. Future investigation of the path of protons from the center of the lipid bilayer to the lumen is warranted.

All rotary ATPase a subunits include an essential Arg residue, Arg735 in the *S. cerevisiae* V-ATPase, which is necessary for coupling ATP synthesis or hydrolysis to proton translocation^{26,27}. The conserved Glu residues of subunits c, c', and c'' are also essential for proton transport in the V-ATPase¹³. The auto-inhibited V_O complex is stopped with Glu108 of subunit c'' interacting with Arg735 on the penultimate α -helix of subunit a⁵ (Fig. 3C). This interaction suggests that Glu108 is deprotonated. The presumed salt bridge between Arg735 and Glu108 is similar to Arg-Asp pairs that have been observed to ensure proton selectivity in voltage-gated proton channels²⁸. However, some rotary ATPases transport other ions and the architecture of rotary ATPases appears to be generally conserved. Therefore, the Arg-Glu pair here likely ensures that the Glu residue is stripped of its ion before leaving the luminal half-channel, rather than ensuring proton specificity.

Subunits e and f

LC MS/MS analysis of in-gel digested protein suggested that Vma9p (subunit e) and putative protein YPR170W-B were present in the purified V_O complex (Supplementary Table. 2). The α -helical hairpin shown in blue in Fig. 1A-C was identified as subunit e because its density fit with the three Trp residues and Phe and Tyr residues of subunit e (Supplementary Fig. 3E). The structure of subunit e and the interaction of its C terminus with a loop in subunit a explains why addition of a C-terminal affinity tag to subunit e causes its dissociation from the detergent-solubilized complex²⁹. Its position distal to the interaction of subunit a and the c-ring is consistent with the observation that it can be removed from the assembled V-ATPase without affecting proton-pumping activity. Deletion of the VMA9 gene leads to the conditionally lethal VMA phenotype³⁰ and the absence of V-ATPase from the yeast vacuole, suggesting that subunit e is necessary for successful localization and assembly of the complex³¹. To confirm the presence of putative protein YPR170W-B as the additional membrane-embedded component of the V_O complex, we constructed an *S. cerevisiae* strain with a 3 \times FLAG tag fused to the C

terminus of YPR170W-B. Affinity purification from the detergent solubilized membranes of this strain isolated the V_o complex with some subunits from the intact V-ATPase (Supplementary Fig. 6A), confirming the protein as a component of the V_o complex. We subsequently purified the V_o complex from a yeast strain lacking YPR170W-B and determined its structure by cryo-EM (Supplementary Fig. 6B). The missing density in the 3D map allowed us to unambiguously locate YPR170W-B in the complex. Deletion of YPR170W-B, which we now tentatively identify as subunit f of the V-ATPase, did not produce the *VMA* phenotype³⁰ (Supplementary Fig. 6C) showing that it is not essential for V-ATPase localization or proton pumping. The peripheral location of the protein, away from the subunit a/c-ring interface, leaves its function in the V-ATPase complex unclear, but it may be involved in some of the roles of the V-ATPase beyond proton pumping³². A BLAST search indicates that YPR170W-B is highly conserved in fungi. Reliable identification of possible homologues in the V-ATPase from animals and plants will require experiments with other organisms. The cryo-EM density for YPR170W-B (red-brown in Fig. 1) had insufficient resolution to build an atomic model and consequently this component of the complex was modeled as poly-alanine.

Mechanism of proton pumping

The asymmetric distribution of Glu residues around the c-ring and how the ring interacts with subunit a has profound implications for possible modes of proton translocation. The spacing between Glu residues in the c-ring has an increment of 36° between most Glu residues, but 18° between the Glu residues of subunits c'' and $c_{(1)}$ (Fig. 2B, purple and light pink), and 54° between the Glu residues of subunits c' and c'' (Fig. 2B, deep pink and purple). As seen in the model, subunit c'' is positioned at the protonating cytoplasmic half-channel (Fig. 4A, blue arrow). In this orientation, subunit $c_{(1)}$ is in contact with subunit a at a possible mid-membrane origin for the luminal half-channel (Fig. 4A, red arrow). However, if the ring were rotated such that one of the c subunits (e.g. subunit $c_{(1)}$) is engaged with the cytoplasmic half-channel (Fig. 4B, blue arrow) then the next c subunit (e.g. subunit $c_{(2)}$) would not be in contact with subunit a, making it unlikely that it is near a luminal half-channel (Fig. 4B, red arrow). Misalignment with any possible luminal half-channel is even more pronounced if subunit c' is engaged with the cytoplasmic half-channel (Fig. 4C, blue arrow), in which case the Glu from subunit c'' is extremely far from contact with subunit a (Fig. 4C, red arrow). This mismatch ensures that protonation and deprotonation cannot always occur simultaneously. Instead, the sequence of events for ATP-hydrolysis driven proton pumping must be that rotation of the c-ring, due to ATP hydrolysis in the V_1 region, breaks the contact of Arg735 with a deprotonated Glu residue and drags the Glu residue into the hydrophobic environment of the lipid bilayer (Fig. 4D). Thermodynamic analysis has shown that moving a deprotonated Glu residue from an aqueous environment into the middle of a lipid bilayer will force the residue to acquire a proton and become neutralized³³. This thermodynamic property of Glu residues ensures that the ring cannot ‘slip’, with a deprotonated Glu moving into the lipid bilayer, which would uncouple ATP hydrolysis from proton pumping. Rotation of the c-ring brings a protonated Glu residue out of the lipid bilayer into alignment with the putative luminal half-channel. Before leaving the luminal half-channel the Glu residue encounters Arg735, possibly in a different orientation than observed in this structure, deprotonating the Glu and resetting the c-ring for a subsequent

protonation-deprotonation cycle. The conformation of Arg735 may also need to adapt to accommodate interaction with the Glu residue of subunit c'' compared to subunit c or c'. The sequence of events, where only one Glu residue at a time interacts with a half-channel, explains how rotary ATPases can tolerate c-rings with variable ²³ and unequal distances between the c-subunits.

Methods

Yeast strains and protein purification: In order to isolate the *S. cerevisiae* V_o complex, yeast strain CACY1, expressing Vph1p (subunit a) with a 3×FLAG tag at its C terminus was prepared by homologous recombination as described previously ⁹. For confirmation that YPR170W-B is a subunit of the V-ATPase, an *S. cerevisiae* strain was prepared with a 3×FLAG tag fused to the C terminus of the uncharacterized open reading frame YPR170W-B (SGD-ID S000028515) in the protease deficient background strain MM93, producing strain SABY87. Purification of intact V-ATPase employed strain SABY31, bearing a 3×FLAG tag on Vma1p and with the STV1 gene deleted ⁹. YPR170W-B was deleted in strain CACY1 by homologous recombination with the NatR cassette to produce strain MMJY1 as described ⁹. Western blotting against 3×FLAG tagged proteins used monoclonal anti-FLAG antibody M2 (Sigma). For protein purification, yeast in YPD medium were grown in an 11 L BioFlo fermenter (New Brunswick Scientific) for 60 h in order to induce nutrient starvation and dissociation of the V_i and V_o regions of the complex. V_o complex solubilized with dodecylmaltoside (DDM) was purified via the 3×FLAG tag with M2 affinity matrix (Sigma) following the same protocol used for the intact V-ATPase ^{3,9}. After purification in elution buffer (50 mM Tris-HCl pH 7.5, 150 mM NaCl, 0.02 % [w/v] DDM, 50 µg/mL 3×FLAG peptide), the V_o complex was mixed with amphipol A8-35 (Anatrace) at a protein:amphipol ratio of 1:10 (w/w) with gentle agitation for 1 h and bafilomycin A1 added to 10 µM (Santa Cruz Biotechnology). Detergent was removed with 15 mg/mL Bio-Beads SM-2 (Bio-rad) at 4 °C overnight. The sample was purified further with a Superdex 200 column previously equilibrated with buffer (50 mM Tris-HCl pH 7.5, 150 mM NaCl). The peak corresponding to the V_o complex was collected and concentrated to 2.5 mg/mL with a 100 kDa MWCO Amicon concentrator (Millipore) for further analysis.

LC-MS/MS and database search: Subunits of the V_o preparation were separated by SDS-PAGE and regions of the gel excised at positions where small trans-membrane α -helical hairpin subunits are expected. Proteins were digested in the gel as described previously ³⁴ with trypsin and chymotrypsin at 37 °C and 25 °C, respectively. For combined tryptic and chymotryptic digestion, proteins were digested with trypsin at 37 °C for three hours before chymotrypsin was added and the sample was incubated at 25 °C overnight. Peptides dissolved in 2 % (v/v) acetonitrile and 0.1 % (v/v) formic acid were separated by nano-flow liquid chromatography (Dionex UltiMate 3000 RSLC, Thermo scientific; mobile phase A: 0.1 % [v/v] formic acid; mobile phase B: 80 % [v/v] acetonitrile, 0.08% [v/v] formic acid). Peptides were then loaded onto a trap column (Reprosil C18, 100 µm I.D., particle size 5µm; Dr. Maisch GmbH, prepared in-house) and separated with a flow rate of 300 nL/min on an analytical C18 capillary column

(Reprosil C18, 75 μ m I.D., particle size 1.9 μ m, 27-28 cm; Dr. Maisch GmbH, prepared in-house), with a gradient of 5-90 % (v/v) mobile phase B over 46 min. Separated peptides were directly eluted into a Orbitrap Fusion Tribrid Mass Spectrometer (Thermo scientific). Typical mass spectrometric conditions were: spray voltage of 2.3 kV; capillary temperature of 275 °C; collision energy of 30 %, activation Q of 0.25. The Orbitrap Fusion Tribrid Mass Spectrometer was operated in data-dependent mode. Survey full scan MS spectra were acquired in the orbitrap (m/z 380–1500) with a resolution of 120,000 and an automatic gain control (AGC) target at 400,000. The top10 most intense ions were selected for HCD MS/MS fragmentation in the orbitrap at a resolution of 30,000 and an AGC target of 1,200 and with a first m/z of 110. Dynamic exclusion of previously selected ions was set to 30 s. Only ions with charge states 2-7 were selected. Singly and doubly charged ions as well as ions with unrecognized charge state were also excluded. Internal calibration of the orbitrap was performed with the lock mass option (lock mass: m/z 445.120025) ³⁵. Raw files were converted into mgf's using Proteome Discoverer (Thermo scientific). Mgf's were searched against Uniprot_Yeast database (23,481 sequences) using Mascot search engine v2.03.2002 (Matrix Science). Search parameters were: Peptide mass tolerance, 10 ppm; fragment mass tolerance, 0.6 Da; enzyme, trypsin; variable modifications, carbamidomethylation (cysteine) and oxidation (methionine).

Cryo-EM and image analysis: V_o complex (2.5 μ L) in amphipol was applied to nanofabricated holey-gold coated EM grids ³⁶ previously glow discharged in air for 15 s, blotted for 15 seconds, and then plunge frozen with a modified Vitrobot grid preparation device (FEI Company) in a mixture of liquid ethane and propane at liquid nitrogen temperature ³⁷. Cryo-EM grid preparation conditions were optimized and a small dataset consisting of 1,082 images obtained with a field-emission Tecnai F20 electron microscope (FEI Company) operating at 200 kV, with images recorded on a Gatan K2 Summit (Gatan Inc) direct detector device camera (counting mode, 2 frames/s, 15 s, 1.45 Å/pixel, 1.2 electrons/pixel/frame). An initial model for the V_o complex was generated by manually segmenting a map of the intact V-ATPase ¹ with *UCSF Chimera* ³⁸ and low-pass filtering to 30 Å. Image analysis with *Alignframes_lmbfgs* ³⁹, *CTFFIND3* ⁴⁰, *Alignparts_lmbfgs* ³⁹, magnification anisotropy correction ⁴¹ and *Relion 1.3* ⁴² produced a preliminary map at 6.8 Å resolution from 39,384 particle images. The structure of the V_o complex in DDM was also determined from yeast strains CACY1 (wild type) and MMJY1 (Δ YPR170W-B). These specimens were prepared with nanofabricated holey-carbon coated EM grids subjected to glow discharge for 2 min and blotted for 20 s. 3D maps were calculated at 8.3 Å resolution from 43,184 particle images (CACY1) and 8.7 Å resolution from 44,468 particle images (MMJY1).

For high-resolution image acquisition, grids were sent in a cryogenic specimen shipper to the HHMI Janelia Research Campus where they were imaged with a Titan Krios electron microscope (FEI Company). Micrographs were recorded from a single grid with the microscope operated at 300 kV using parallel illumination at 4.8 e⁻/Å²/s of a 1.58 μ m diameter region of the grid from a 70 μ m objective aperture. Images were recorded with a K2 Summit direct detector device camera operating in super-resolution mode with a nominal magnification of 37,000 \times . With no specimen present in the optical path, the rate

of exposure of the detector was 3 electrons/pixel/s. Dose-fractionated exposures of 21 s were recorded as movies with 70 frames, so that selected specimen areas were exposed to a total of 100 electrons/Å². Data collection was automated with *SerialEM*⁴³. A previously measured magnification anisotropy was corrected with the program *mag_distortion_correct*⁴⁴, leading to a super-resolution pixel size of 0.3885 Å. Frames were down-sampled to a pixel size of 1.554 Å by Fourier-space cropping and aligned with each other using *Unblur*⁴⁵. Likely because of the high magnification and small field of view, no apparent advantage was detected for correcting images for individual particle motion³⁹. Defocus parameters were estimated with *CTFFIND4*⁴⁶ from the average of amplitude spectra of sums of 3 unaligned frames resampled to a pixel size of 1.94 Å. 657,975 particle images were automatically selected with *Relion* from 4,365 aligned and averaged movies, and extracted into 200×200 pixel boxes. 2D classification with *Relion* reduced the dataset to 462,842 particle images.

The map showing the V_O complex lacking subunit d was obtained by 3D classification and refinement with *Relion 1.3*⁴². The 6.8 Å resolution map of the V_O complex in amphipol from the Tecnai F20 dataset was used as a starting reference for aligning the full dataset of particle images with *Frealign*⁴⁷. In all subsequent processing steps, information beyond 6 Å resolution was excluded to prevent over-fitting of noise at higher resolutions. Initial particle orientation parameters were obtained by 1 cycle of grid search in *Frealign*'s mode 3, using an angular step size of 3.4 °. Following this cycle, and before every subsequent cycle, the solvent and amphipol regions of map were low-pass filtered to 30 Å to reduce fitting of noise from solvent and amphipol densities⁴⁸. Final particle orientation parameters were obtained after 19 cycles of local refinement (mode 1), one cycle of mode 3 exhaustive search, and 11 further cycles of local refinement. The final 3D map was calculated from particle images padded with zeroes from 200×200 to 400×400 pixels to mitigate CTF aliasing effects⁴⁹ and was then Fourier cropped to a 200×200×200 voxel volume. Overall resolution of the map was estimated by FSC to be 3.9 Å. Local resolution variability was estimated with blocres⁵⁰.

Model building: Most regions of the map, particularly membrane-embedded α-helices, had sufficient details to allow *de novo* model building. Initial models for subunits c, c', c'', d, and the N-terminal domain of subunit a were generated with the *SWISS-MODEL* server⁵¹ using PDB 3J9V as a template. The initial model for the membrane-embedded domain of subunit a was from the cryo-EM and evolutionary covariance analysis of that protein⁵. Initial models for subunits e and f were generated manually in *Coot*⁵². Initial models were fit into density as rigid bodies with *UCSF Chimera*³⁸. Final models were built with successive rounds of real space refinement in *Phenix*⁵³ and manual model building in *Coot* and gave an *EMRinger* score of 2.2 for the entire model⁵⁴, which is superior to the typical score of 1.0 for a 4 Å map. 93.2, 6.3, and 0.5 % of residues were in preferred, allowed, and disallowed regions of Ramachandran plot, respectively, with no Ramachandran outliers in the α-helical regions of the model. Where no corresponding densities were observed, side chains were deleted while maintaining the residue identity. Subunit f and the N-terminal domain of subunit a were modeled entirely as poly-alanine.

Acknowledgements

We thank Nikolaus Grigorieff for providing access to the Titan Krios electron microscope and Henning Urlaub for providing CS with access to mass spectrometry instrumentation while in Göttingen. We thank Zev Ripstein, Peter Tieleman, Régis Pomès, and Jean-Philippe Julien for discussions, and Jianhua Zhao, Jean-Philippe Julien, and Voula Kanelis for a critical reading of the manuscript. MTMJ was supported by a Postdoctoral Fellowship from the Canadian Institutes of Health Research (CIHR), CVR is a Royal Society Professor and JLR holds a Canada Research Chair. This work was supported by operating grant MOP81294 from the Canadian Institutes of Health Research (JLR), Wellcome Trust grants WT008150 and WT099141 (CVR), and European Research Council IMPRESS grant ERC268851 (CVR).

Author contributions

MTMJ prepared yeast strains, purified protein, prepared cryo-EM specimens, did 200 kV cryo-EM and *Relion* image analysis, and built the atomic models. AR collected data with the 300 kV microscope and did image analysis with *Frealign*. CS performed the mass spectrometry analysis. SAB prepared yeast strains and assisted with protein purification. SB assisted with cryo-EM specimen preparation and screening. CVR supervised mass spectrometry experiments and JLR supervised the other aspects of the work and coordinated experiments. JLR and MTMJ wrote the manuscript and prepared the figures with input from the other authors.

Figure Captions

Figure 1. The intact V_o complex. **A**, The V_o cryo-EM density map (mesh, upper) shows subunits a (green), c (pink), c' (deep pink), c'' (purple), d (cyan), e (blue), and f (red-brown). The '*' indicates the contact between subunits d and c''. **B** and **C**, enlarged view and cartoon of the C-terminal domain of subunit a with subunits e and f. Unfitted density is in grey. **D**, The cryo-EM map allows atomic models to be built for most of the protein sequence. Scale bars, 25 Å.

Figure 2. Asymmetry of the c-ring. **A**, A model of the c-ring (left) with a map section (right) shows the two N-terminal α -helices of subunit c'' in the middle of the c-ring. **B**, A view of the c-ring model (left) and cartoon (right) from the cytoplasm shows the asymmetric distribution of mid-membrane Glu residues around the ring. The two N-terminal α -helices of subunit c'' are marked with a '*' (left). Scale bars, 25 Å.

Figure 3. Cytoplasmic half-channel and subunit a/c-ring interaction. **A** and **B**, a large cavity (blue density and arrow) is apparent between the c-ring and subunit a in the expected position of the cytoplasmic half-channel. The cavity is near the unresolved loop composed of residues 659 to 709 from subunit a (lower, broken red line). Scale bar, 25 Å. **C**, At the mid-membrane terminus of the cavity, the essential residues Arg735 from subunit a and Glu108 from subunit c'' are positioned to interact.

Figure 4. Irregularly spaced Glu residues require protonation before deprotonation. **A**, The observed structure (upper) with cartoon (lower) shows that when Glu108 of

subunit c'' is aligned with the cytoplasmic half-channel (blue arrow), Glu137 of subunit $c_{(1)}$ contacts subunit a (red arrow) and could be aligned with a luminal half-channel. **B**, When Glu137 of a c subunit is aligned with the cytoplasmic half-channel (blue arrow) Glu137 of the next c subunit is not in contact with subunit a (red arrow). **C**, When Glu145 of subunit c' is aligned to the cytoplasmic half-channel (blue arrow) Glu108 of subunit c'' is too far from subunit a to interact (red arrow). Scale bar, 25 Å. **D**, Sequence of protonation and deprotonation events that occur during c -ring rotation, with each Glu residue given a unique colour.

References

1. Zhao, J., Benlekbir, S. & Rubinstein, J. L. Electron cryomicroscopy observation of rotational states in a eukaryotic V-ATPase. *Nature* **521**, 241–245 (2015).
2. Allegretti, M. *et al.* Horizontal membrane-intrinsic alpha-helices in the stator a-subunit of an F-type ATP synthase. *Nature* **521**, 237–240 (2015).
3. Zhou, A. *et al.* Structure and conformational states of the bovine mitochondrial ATP synthase by cryo-EM. *Elife* **4**, 1–15 (2015).
4. Morales-rios, E., Montgomery, M. G., Leslie, A. G. W. & Walker, J. E. Structure of ATP synthase from *Paracoccus denitrificans* determined by X-ray crystallography at 4.0 Å resolution. *Proc. Natl. Acad. Sci.* **112**, 201517542 (2015).
5. Schep, D. G., Zhao, J. & Rubinstein, J. L. Models for the a subunits of the *Thermus thermophilus* V/A-ATPase and *Saccharomyces cerevisiae* V-ATPase enzymes by cryo-EM and evolutionary covariance. *Proc. Natl. Acad. Sci.* 201521990 (2016). doi:10.1073/pnas.1521990113
6. Kane, P. M. Disassembly and reassembly of the yeast vacuolar H(+)-ATPase in vivo. *J Biol Chem* **270**, 17025–17032 (1995).
7. Sumner, J. P. *et al.* Regulation of plasma membrane V-ATPase activity by dissociation of peripheral subunits. *J Biol Chem* **270**, 5649–5653 (1995).
8. Couoh-Cardel, S., Milgrom, E. & Wilkens, S. Affinity purification and structural features of the yeast vacuolar ATPase Vo membrane sector*. *J. Biol. Chem.* **290**, 27959–27971 (2015).
9. Benlekbir, S., Bueler, S. A. & Rubinstein, J. L. Structure of the vacuolar-type ATPase from *Saccharomyces cerevisiae* at 11-Å resolution. *Nat Struct Mol Biol* **19**, 1356–1362 (2012).
10. Qi, J. & Forgac, M. Function and subunit interactions of the N-terminal domain of subunit a (Vph1p) of the yeast V-ATPase. *J Biol Chem* **283**, 19274–19282 (2008).
11. Zhou, Q., Petersen, C. C. & Nicoll, R. A. Effects of reduced vesicular filling on synaptic transmission in rat hippocampal neurones. *J. Physiol.* **525 Pt 1**, 195–206 (2000).
12. Powell, B., Graham, L. a & Stevens, T. H. Molecular characterization of the yeast vacuolar H+-ATPase proton pore. *J. Biol. Chem.* **275**, 23654–60 (2000).
13. Hirata, R., Graham, L. A., Takatsuki, A., Stevens, T. H. & Anraku, Y. VMA11 and VMA16 encode second and third proteolipid subunits of the *Saccharomyces cerevisiae* vacuolar membrane H+-ATPase. *J. Biol. Chem.* **272**, 4795–4803 (1997).
14. Nishi, T., Kawasaki-Nishi, S. & Forgac, M. The first putative transmembrane segment of subunit c" (Vma16p) of the yeast V-ATPase is not necessary for function. *J. Biol. Chem.* **278**, 5821–7 (2003).
15. Couoh-Cardel, S., Hsueh, Y.-C., Wilkens, S. & Movileanu, L. Yeast V-ATPase Proteolipid Ring Acts as a Large-conductance Transmembrane Protein Pore. *Sci. Rep.* **6**, 24774 (2016).
16. Matthies, D. *et al.* High-resolution structure and mechanism of an F/V-hybrid rotor ring in a Na(+)-coupled ATP synthase. *Nat. Commun.* **5**, 5286 (2014).
17. Vik, S. & Antionio, B. J. A mechanism of proton translocation by F1F0 ATP synthases suggested by double mutants of the a subunit. *J Biol Chem* **269**, 30364–9. (1994).

18. Junge, W., Lill, H. & Engelbrecht, S. ATP synthase: an electrochemical transducer with rotatory mechanics. *Trends Biochem Sci* **22**, 420–423 (1997).
19. Neale, C., Chakrabarti, N., Pomorski, P., Pai, E. F. & Pom??s, R. Hydrophobic Gating of Ion Permeation in Magnesium Channel CorA. *PLoS Comput. Biol.* **11**, 1–22 (2015).
20. Angevine, C. M., Herold, K. a G. & Fillingame, R. H. Aqueous access pathways in subunit a of rotary ATP synthase extend to both sides of the membrane. *Proc. Natl. Acad. Sci. U. S. A.* **100**, 13179–13183 (2003).
21. Angevine, C. M. & Fillingame, R. H. Aqueous access channels in subunit a of rotary ATP synthase. *J Biol Chem* **278**, 6066–6074 (2003).
22. Toei, M., Toei, S. & Forgac, M. Definition of membrane topology and identification of residues important for transport in subunit a of the vacuolar ATPase. *J Biol Chem* **286**, 35176–35186 (2011).
23. Kuhlbrandt, W. & Davies, K. M. Rotary ATPases: A New Twist to an Ancient Machine. *Trends Biochem. Sci.* **41**, 106–116 (2016).
24. Pellegrini-Calace, M., Maiwald, T. & Thornton, J. M. PoreWalker: A novel tool for the identification and characterization of channels in transmembrane proteins from their three-dimensional structure. *PLoS Comput. Biol.* **5**, (2009).
25. Smart, O. S., Neduvélil, J. G., Wang, X., Wallace, B. A. & Sansom, M. S. P. HOLE: A program for the analysis of the pore dimensions of ion channel structural models. *J. Mol. Graph.* **14**, 354–360 (1996).
26. Kawasaki-Nishi, S., Nishi, T. & Forgac, M. Arg-735 of the 100-kDa subunit a of the yeast V-ATPase is essential for proton translocation. *Proc Natl Acad Sci U S A* **98**, 12397–12402 (2001).
27. Cain, B. D. & Simoni, R. D. Impaired proton conductivity resulting from mutations in the a subunit of F1F0 ATPase in Escherichia coli. *J. Biol. Chem.* **261**, 10043–10050 (1986).
28. Decoursey, T. E. The voltage-gated proton channel: A riddle, wrapped in a mystery, inside an enigma. *Biochemistry* **54**, 3250–3268 (2015).
29. Bueler, S. A. & Rubinstein, J. L. Vma9p Need Not Be Associated with the Yeast V-ATPase for Fully-Coupled Proton Pumping Activity in Vitro. *Biochemistry* **54**, 853–858 (2015).
30. Nelson, H. & Nelson, N. Disruption of genes encoding subunits of yeast vacuolar H(+)-ATPase causes conditional lethality. *Proc. Natl. Acad. Sci. U. S. A.* **87**, 3503–7 (1990).
31. Compton, M. A., Graham, L. A. & Stevens, T. H. Vma9p (subunit e) is an integral membrane V0 subunit of the yeast V-ATPase. *J Biol Chem* **281**, 15312–15319 (2006).
32. Kane, P. M. The long physiological reach of the yeast vacuolar H⁺-ATPase. *J Bioenerg Biomembr* **39**, 415–421 (2007).
33. MacCallum, J. L., Bennett, W. F. D. & Tieleman, D. P. Distribution of amino acids in a lipid bilayer from computer simulations. *Biophys. J.* **94**, 3393–3404 (2008).
34. Shevchenko, A., Wilm, M., Vorm, O. & Mann, M. Mass spectrometric sequencing of proteins from silver-stained polyacrylamide gels. *Anal. Chem.* **68**, 850–858 (1996).

35. Olsen, J. V *et al.* Parts per million mass accuracy on an Orbitrap mass spectrometer via lock mass injection into a C-trap. *Mol Cell Proteomics* **4**, 2010–2021 (2005).
36. Marr, C. R., Benlekbir, S. & Rubinstein, J. L. Fabrication of carbon films with approximately 500 nm holes for cryo-EM with a direct detector device. *J Struct Biol* **185**, 42–47 (2014).
37. Tivol, W. F., Briegel, A. & Jensen, G. J. An improved cryogen for plunge freezing. *Microsc. Microanal.* **14**, 375–379 (2008).
38. Goddard, T. D., Huang, C. C. & Ferrin, T. E. Visualizing density maps with UCSF Chimera. *J Struct Biol* **157**, 281–287 (2007).
39. Rubinstein, J. L. & Brubaker, M. A. Alignment of cryo-EM movies of individual particles by optimization of image translations. *J. Struct. Biol.* **192**, 188–95 (2015).
40. Mindell, J. A. & Grigorieff, N. Accurate determination of local defocus and specimen tilt in electron microscopy. *J Struct Biol* **142**, 334–347 (2003).
41. Zhao, J., Brubaker, M. A., Benlekbir, S. & Rubinstein, J. L. Description and comparison of algorithms for correcting anisotropic magnification in cryo-EM images. *J. Struct. Biol.* **192**, 209–15 (2015).
42. Scheres, S. H. W. RELION: Implementation of a Bayesian approach to cryo-EM structure determination. *J Struct Biol* **180**, 519–530 (2012).
43. Mastronarde, D. N. Automated electron microscope tomography using robust prediction of specimen movements. *J Struct Biol* **152**, 36–51 (2005).
44. Grant, T. & Grigorieff, N. Automatic estimation and correction of anisotropic magnification distortion in electron microscopes. *J. Struct. Biol.* 6–10 (2015). doi:10.1016/j.jsb.2015.08.006
45. Grant, T. & Grigorieff, N. Measuring the optimal exposure for single particle cryo-EM using a 2.6 Å reconstruction of rotavirus VP6. *Elife* **4**, e06980 (2015).
46. Rohou, A. & Grigorieff, N. CTFFIND4: Fast and accurate defocus estimation from electron micrographs. *J. Struct. Biol.* 5–10 (2015). doi:10.1016/j.jsb.2015.08.008
47. Grigorieff, N. FREALIGN: high-resolution refinement of single particle structures. *J Struct Biol* **157**, 117–125 (2007).
48. Grigorieff, N. *Frealign: An Exploratory Tool for Single-Particle Cryo-EM. Resolut. Revolut. Recent Adv. cryoEM* (Elsevier Inc., 2016). doi:10.1016/bs.mie.2016.04.013
49. Penczek, P. A. *et al.* CTER-Rapid estimation of CTF parameters with error assessment. *Ultramicroscopy* **140**, 9–19 (2014).
50. Cardone, G., Heymann, J. B. & Steven, A. C. One number does not fit all: Mapping local variations in resolution in cryo-EM reconstructions. *J. Struct. Biol.* **184**, 226–236 (2013).
51. Arnold, K., Bordoli, L., Kopp, J. & Schwede, T. The SWISS-MODEL workspace: A web-based environment for protein structure homology modelling. *Bioinformatics* **22**, 195–201 (2006).
52. Emsley, P. & Cowtan, K. Coot: Model-building tools for molecular graphics. *Acta Crystallogr. Sect. D Biol. Crystallogr.* **60**, 2126–2132 (2004).
53. Adams, P. D. *et al.* PHENIX: A comprehensive Python-based system for macromolecular structure solution. *Acta Crystallogr. Sect. D Biol. Crystallogr.* **66**, 213–221 (2010).

54. Barad, B. A. *et al.* EMRinger: side chain-directed model and map validation for 3D cryo-electron microscopy. *Nat. Methods* **12**, 943–6 (2015).

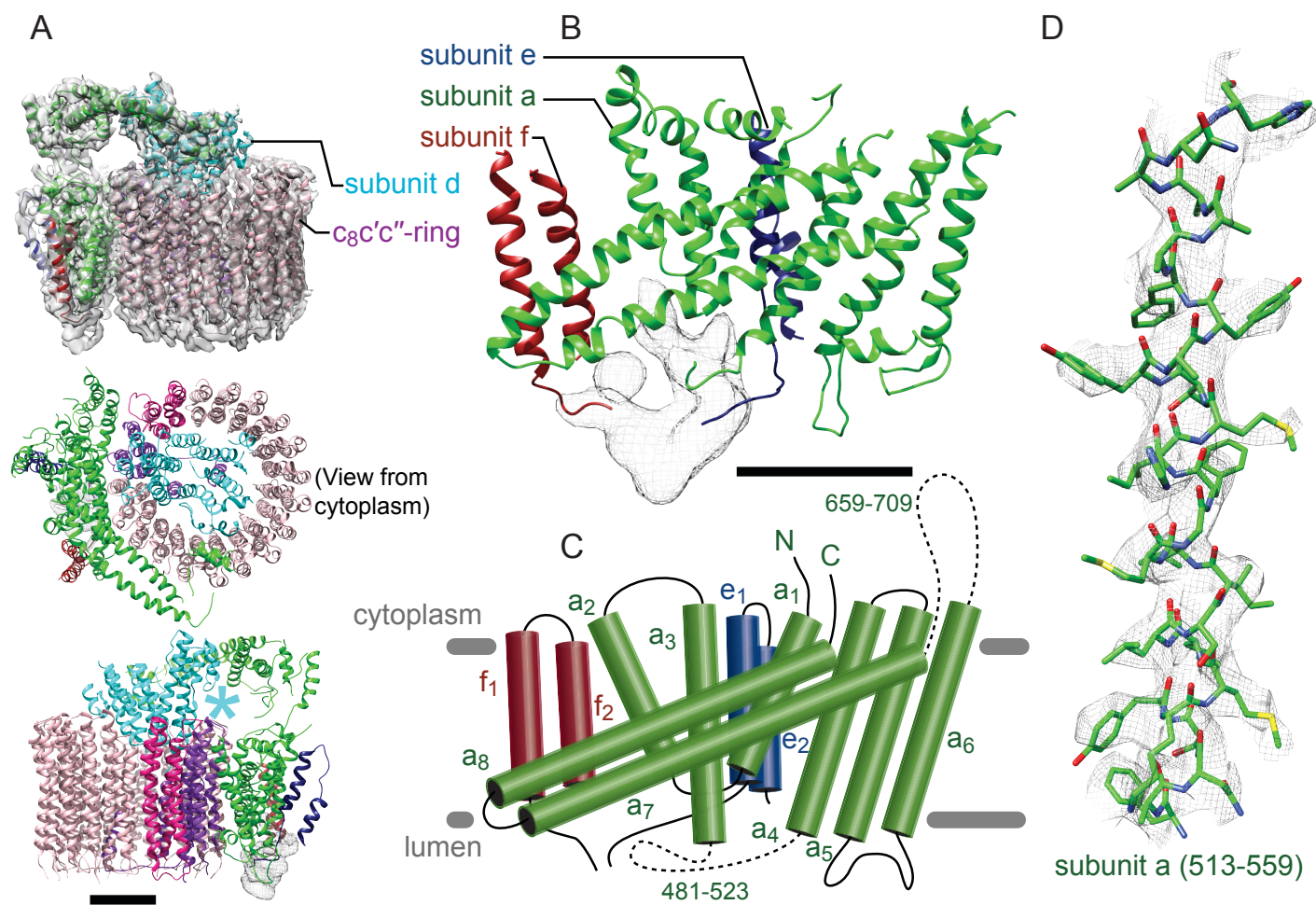


Fig. 1

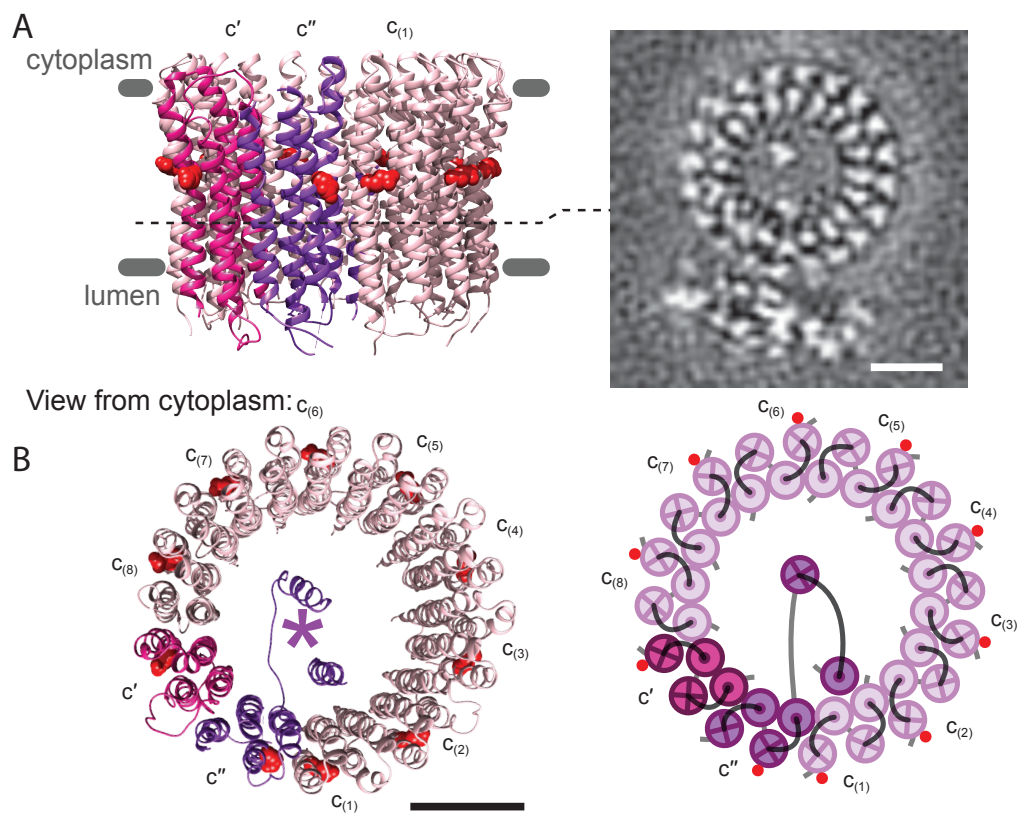


Fig. 2

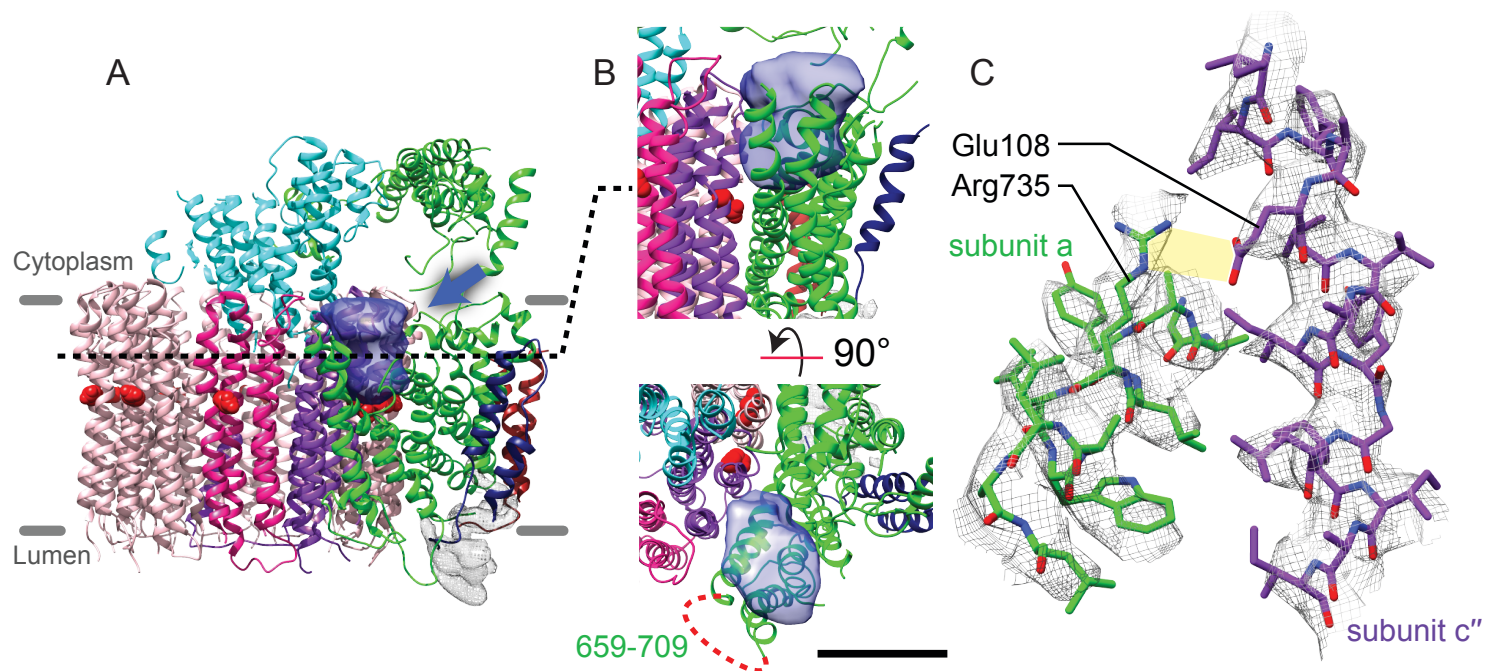


Fig. 3

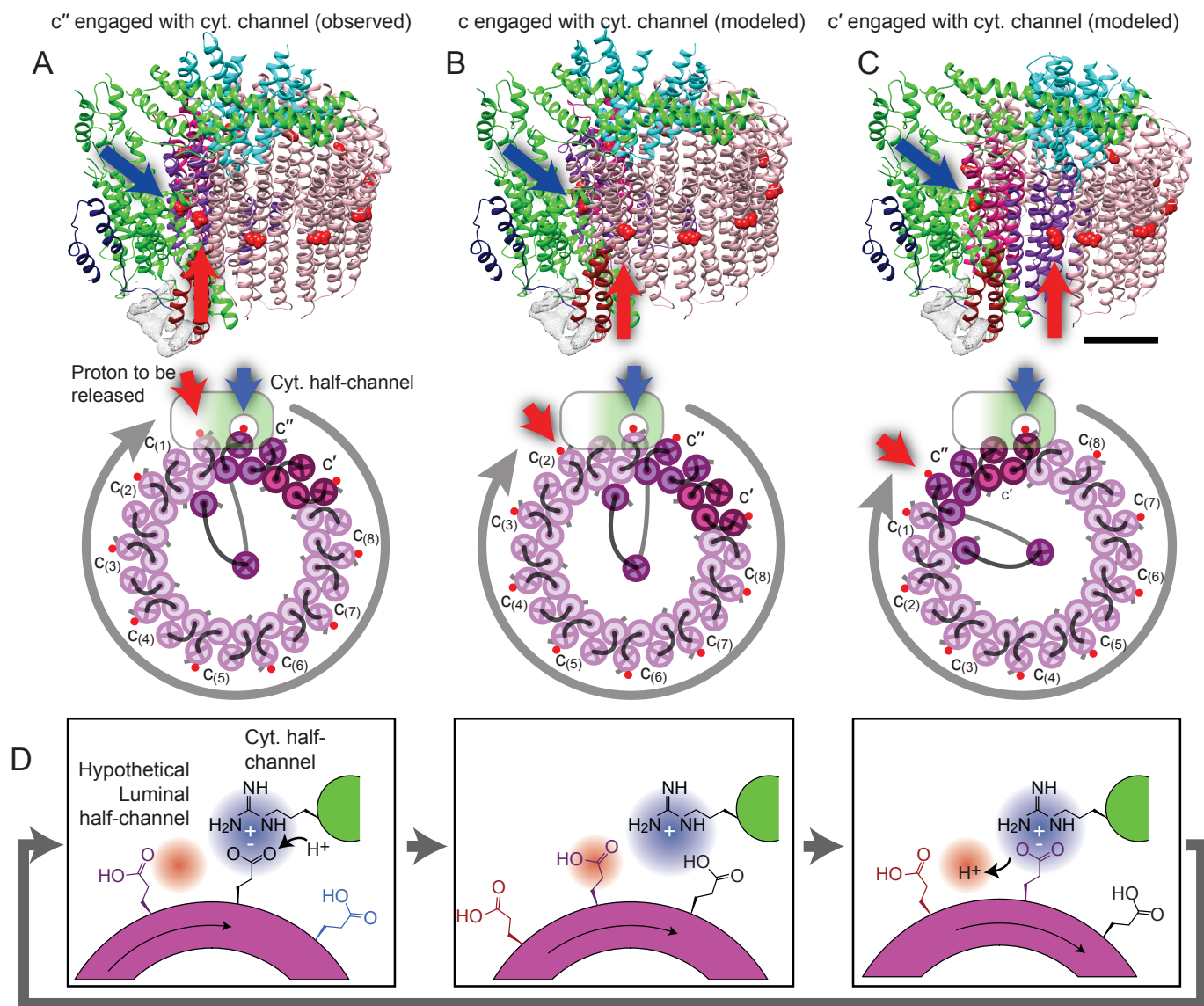


Fig. 4